The influence of hydrogen on the stability of a perfectly premixed combustor

José G. Aguilar, Eirik Æsøy*, James R. Dawson

Institute for Energy and Process Engineering, Norwegian University of Science and Technology (NTNU). Strømningsteknisk Kolbjørn Hejesvei 2, Trondheim 7491, Norway

ABSTRACT

In this paper we investigate the effects of increasing the amount of hydrogen in the fuel mixture on the stability of a perfectly premixed combustor. Experiments are carried out on a single flame burner where the thermal power and equivalence ratio are kept constant while the amount of hydrogen is progressively increased from pure methane towards higher fractions of $CH_4 - H_2$ blends. As hydrogen content is increased, the flame first experiences a series of topological changes until the system becomes unstable and a limit cycle is established. The changes experienced by the flame occur due to the increased burning speed of the mixture which shortens the flame. The flame changes from a lifted flame attached to the combustor wall, to a bluff body anchored flame also attached to the wall, to a bluff body anchored flame detached from the wall. For some $CH_4 - H_2$ mixture fractions, there exists a bi-stable region where the last two flame shapes can be observed at the same operating conditions. As for the observed limit cycle, first a low amplitude limit cycle is established and a further increase in hydrogen content leads to a much higher amplitude one.

The linear stability limit is predicted using a low-order network model where the flame response is modeled by a scaled distributed time lag model which provides good agreement with the experimental observations. The flame model only requires a measurement of the flame length and bulk velocities which significantly simplify the analysis when considering operating conditions where the flame transfer function has not been measured. In the region where the flame is bi-stable, the linear stability analysis shows that the flame attached to the combustor wall becomes unstable at lower hydrogen content when compared to the flame detached from the combustor wall. Therefore, from a linear stability perspective and in line with experimental observations, the flame changes shape in order to keep the system stable. Furthermore, a nonlinear model using the flame describing function approach is also implemented to analyze the transition between the two limit-cycles. The analysis shows that the system has a low amplitude stable limit cycle and a neighbouring unstable limit cycle with a slightly higher amplitude. This shows that the system is triggering until full saturation occurs at the much higher amplitude limit cycle, consistent with the experimental observations. The analysis presented in this paper demonstrates that the effect of premixed hydrogen on thermoacoustic instabilities can be predicted using well established methods.

1. Introduction

One pathway to decarbonize power generation and propulsion is to shift from burning hydrocarbon based fuels to burn hydrogen, which can be produced from the excess energy of renewable sources. However, the thermo-chemical properties of hydrogen are very different when compared to typical hydrocarbons. For instance, its laminar burning speed can be up to an order of magnitude different compared to methane [1–3]. These properties may introduce new challenges for combustion systems such as thermoacoustic instabilities or flame flashback, thus requiring a redesign or adaptation of the devices to ensure a stable operation [4–7].

Recent studies show that the effect of hydrogen in combustion dynamics depends considerably on the way it is introduced into the system. We identify three different categories:

- *Pure hydrogen pilot fuel injection.* Using a very small amount of pure hydrogen in a pilot flame Oztarlik et al. [8] stabilized a methane flame in a swirl combustor. They also found that if the

same amount of hydrogen was added to the methane-air mixture, the stabilizing effect was not achieved. This phenomenon was further investigated by Schuller et al. [9] by analysing the flame describing function of such flames and by Laera et al. [10] using LES.

- *Lean-premixed pure hydrogen flames.* On an injector geometry consisting of an array with multiple nozzles Lee and Kim [11] and Kang and Kim [12] found that lean-premixed pure hydrogen flames were able to excite the high frequency modes of the combustor (up to 1800 Hz). Lee and Kim [13] found that even higher frequencies (up to 3.5 kHz) could be excited using a multi-slit injector.

- *Lean-premixed H_2-hydrocarbon flames.* Figura et al. [14] found that increased levels of hydrogen content may shift the instability regions to lower equivalence ratios or flame temperatures. In swirl configurations, several authors [15–20] reported that adding hydrogen to a hydrocarbon flame leads to a change in the flame shape. However, the overall effect on the combustion instabilities was different in each case. In a non-swirl configuration Æsøy et al. [21–24] Æsøy [25] showed that increasing hydrogen content leads to more compact flames when compared to hydrocarbon (methane) flames. This results in flame transfer functions (FTFs) with shorter convection time scales and an increase in the cut off frequency which may alter the phase relationship between pressure and unsteady heat release fluctuations leading to thermoacoustic instabilities. In laminar slit flames Ghani and Polifke [26] studied the effect of hydrogen addition in the FTF to control intrinsic thermoacoustic modes. They report that the phase lag of the FTF decreases as hydrogen content increases, in line with the previous references.

Evidently in terms of combustion dynamics the effect of using or adding hydrogen to a flame was different. Therefore, existing combustion systems that operate on hydrocarbons that wish to shift towards burning hydrogen require a careful examination of the flame behavior in order to inform the possible adaptation paths of the system.

Due to its predicting capabilities, accurate modelling of a combustor can aid in taking informed decisions about possible modifications. We distinguish between two different types of modelling approaches: low order models and high fidelity simulations. On the one hand, low order models [27] are very versatile due to their speed and reliability [28]. However, in order to predict thermoacoustic instabilities they typically require precise knowledge of the FTF which may depend on a wide range of parameters [29]. On the other hand, high fidelity simulations [30], however more exact, require more computational resources. These modelling approaches are well established and have been validated against experiments for conventional fuels [31]. However, their applicability when operating with hydrogen is a matter of ongoing research.

This paper aims to bridge the understanding of the effect of hydrogen addition on a methane flame, by linking the experimental observations and measurements, which include flame shape transitions, to a model that can then be used to predict the stability properties of a laboratory scale combustor. To model the combustor, we use the low order network model described in Dowling and Stow [32]. To model the FTF, we use the distributed time lag model from Æsøy et al. [21]. We provide as an input to this model the flame length obtained from mean flame images, and the bulk velocity at the dump plane. This allows us to include the effects of changing operating conditions, including variations in hydrogen content. Besides validating the use of a network model with a distributed time lag model for hydrogen flames (which has been done befor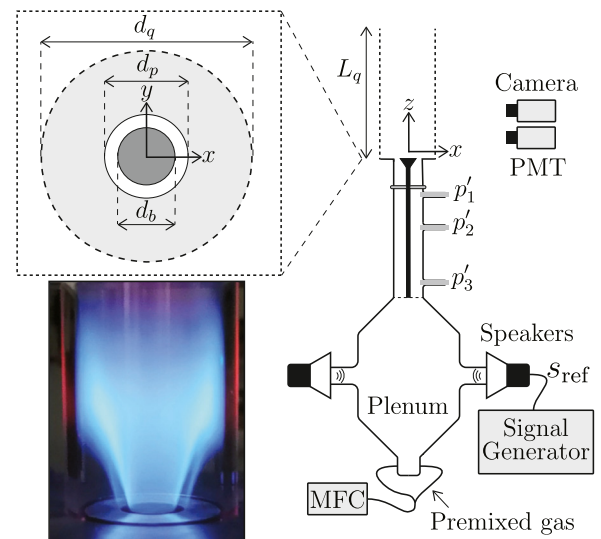e for convectional fuels [33]), the forthcoming analysis provides an insight, from a stability perspective, of the transition in flame shape.

The paper is structured as follows. First the experimental set up and the observations are described. Then we perform an analysis in the linear regime, where we characterize the stability of the combustor as hydrogen content is increased. Finally, we perform a nonlinear analysis using the describing function approach to delve into the features of the observed limit cycle.

Fig. 1. Experimental set-up. For more details the reader is referred to [21,25].

2. Experimental set-up and operating conditions

Figure 1 shows a schematic of the experimental set-up which is the same as in [21]. Flames are stabilized on a bluff body with diameter $d_b = 13$ mm, centred on a rod of diameter $d_r = 5$ mm inside a pipe of diameter $d_p = 19$ mm. The combustion chamber is a circular quartz tube of diameter $d_q = 44$ mm with a total length $L_q = 80$ mm or $L_q = 150$ mm. The former is used to avoid self excited combustion instabilities. The injector pipe is connected to a plenum upstream where the flow is conditioned. To acoustically force the flame, two Monacor KU-516 (75W, 16Ω) horn drivers are mounted as indicated on the schematic. An Aim-TTi TGA1244 40MHz signal generator (SG) is used to generate harmonic forcing signals, s_{ref}, which are amplified by a QTX Sound PRO1000 power amplifier. The air and fuel mass flow rates are controlled individually using Alicat mass flow controllers (MFCs) with a variation in the flow rates of less than $\pm 1\%$. All gases are mixed sufficiently far upstream to ensure that the mixture is fully premixed. The total mass flow rate $\dot{m}_{MFC}$ is measured by the MFCs and the mean bulk velocity $\bar{u}$ at various locations in the combustor is estimated from a mass balance.

2.1. Measurements

A Cartesian coordinate system (x, y, z) is defined with the origin located at the centre of the bluff-body as indicated in Fig. 1. The acoustic pressure p'_i is measured at three axial positions denoted z_i for $i = 1, 2, 3$ in the injector pipe by Kulite XCS-093-0.35D pressure transducers. The global heat release rate is measured using a Hamamatsu H11902-113 PMT equipped with a UV band pass filter (310(10)nm). Following previous studies of perfectly premixed flames [29,34–36], the unsteady rate of heat release is assumed to be proportional to the light emitted by excited OH* radicals, thus
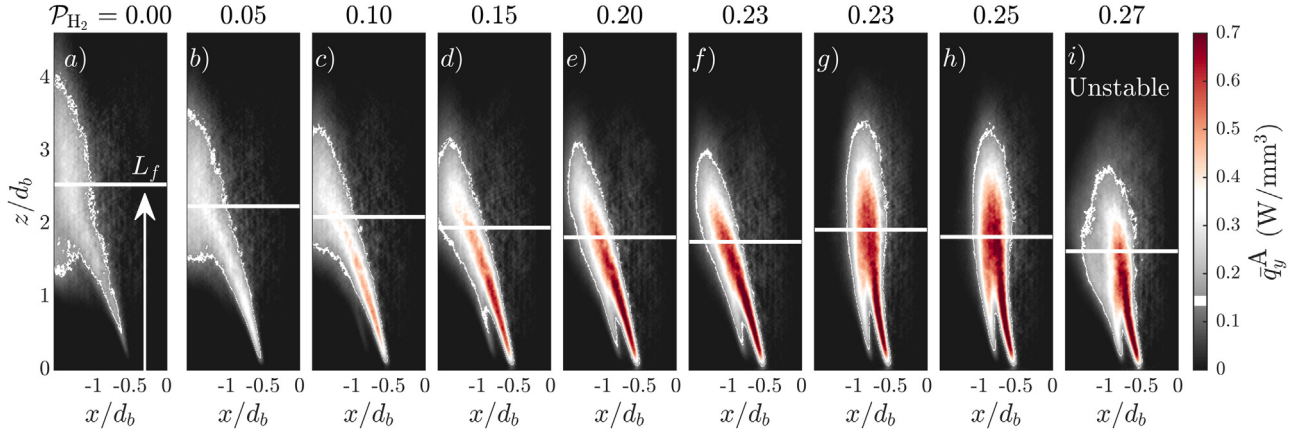
Fig. 2. Abel deconvoluted mean flame images $\bar{q}_y^A$ shown for $x/d_b < 0$ corresponding to experimental set A. Operating conditions: $P = 7$ kW, $\phi = 0.7$, $L_q = 150$ mm, and increasing hydrogen content $\mathcal{P}_{H_2}$. As $\mathcal{P}_{H_2}$ increases the flame progressively stabilizes closer to the bluff body. At $\mathcal{P}_{H_2} = 0.27$ the system becomes self-excited.

Table 1

Operating conditions in terms of power fraction of hydrogen, $\mathcal{P}_{H_2}$, volume fraction of hydrogen, $\mathcal{V}_{H_2}$, bulk velocity $\bar{u}$ at the dump plane, combustion chamber length, L_q and equivalence ratio ϕ. For all cases $P = 7$ kW.

Set	$\mathcal{P}_{H_2}$ [%]	$\mathcal{V}_{H_2}$ [%]	$\bar{u}$ [m/s]	ϕ	L_q [mm]	FTF
A	$0 - 35$	$0 - 62$	$20.7 - 20.1$	0.7	150	✗
B	$0 - 40$	$0 - 67$	$20.7 - 20.0$	0.7	80	✓
C	30	57	23.1	0.6	80	✓

$I'/\bar{I} = Q'/\bar{Q}$, where I is the PMT intensity and Q is the heat release rate. Time series of the reference signal (s_{ref}), pressure, and heat release rate are sampled at a rate of 51.2 kHz and digitized using a 24-bit NI-9234 DAQ.

For high speed flame visualization, we consider $q(x, y, z, t)$ as the spatio-temporal distribution of heat release rate (HRR) and $\bar{q}$ as its temporal average. The line of sight integrated heat release rate $q_y = \int q \, dy$ is measured using a Phantom V2012 high speed camera equipped with a LaVision Intensified Relay Optics (IRO) unit with a Cerco 2178 UV lens (100F/2.8) and the same band pass filter used on the PMT. The global heat release Q is retrieved from the images by integrating the HRR over the whole volume, i.e., $Q(t) = q_{xyz}(t) = \int_V q \, dV$. The signal from the PMT and q_y are normalized such that $\bar{Q} = \bar{q}_{xyz} = 7$ kW. Assuming an axisymmetric flame, the mean planar HRR is obtained by Abel deconvolution [37] and denoted $\bar{q}_y^A$.

2.2. Operating conditions

The operating conditions considered are summarized in Table 1. Experimental sets A and B are operated with constant thermal power $P = 7$ kW and constant equivalence ratio $\phi = 0.7$ while hydrogen content, here expressed in terms of power fraction of hydrogen $\mathcal{P}_{H_2}$, is progressively increased. Set A uses a combustion chamber length of $L_q = 150$ mm to promote thermo-acoustic instabilities. Set B uses a shorter combustion chamber, $L_q = 80$ mm, to avoid the instabilities and to measure the flame length and the flame response to acoustic fluctuations in the form of a Flame Transfer Function (FTF) and a Flame Describing Function (FDF). Experimental point C is operated with a thermal power of $P = 7$ kW, a reduced equivalence ratio $\phi = 0.6$, a power fraction of $\mathcal{P}_{H_2} = 0.3$ and the short combustor chamber length $L_q = 80$ mm to elaborate on the effect of flame shape transition observed in the experimental sets A and B.

3. Effect of hydrogen addition on the combustor stability

We begin by discussing the effects that an increase in hydrogen content has on the stability of the combustor by focusing our attention to the experimental set A described by the first row in Table 1. Fig. 2 shows the left half of the Abel deconvoluted mean flame images $\bar{q}_y^A$ of the heat release in the $x - z$ plane for increasing values of $\mathcal{P}_{H_2}$. We define a characteristic flame length L_f as the distance between $z = 0$ and the stream-wise centre of intensity [38]:

$$L_f = \frac{\int z \, \bar{q}_{xy} \, dz}{\int \bar{q}_{xy} \, dz}. \tag{1}$$

L_f is indicated in the figure with solid white lines. This length physically represents the distance between the reference point at $z = 0$ and the spatial centroid of the HRR, which is representative of the location of the PMT signal.

For the pure methane flame shown in Fig. 2a, the flame is slightly lifted from the bluff-body and large portions of the flame brush are attached to the combustor wall in the region $1 < z/d_b < 4$. As the amount of hydrogen is increased the flame gradually detaches from the wall and moves closer to the bluff-body. For $\mathcal{P}_{H_2} > 0.05$ it anchors on the lip of the bluff-body at $x/d_b = -0.5$ and $z/d_b = 0$. The HRR per unit volume also increases and becomes more uniformly distributed along the flame front. This effect reduces the characteristic length L_f. At $\mathcal{P}_{H_2} \approx 0.20$, shown in Fig. 2e, the flame brush detaches from the wall. After a slight increase in hydrogen power fraction, $\mathcal{P}_{H_2} = 0.23$, we observe a sudden change in the flame shape which leads to an abrupt increase of L_f, (see Fig. 2f,g). As a matter of fact, in the region $0.19 < \mathcal{P}_{H_2} < 0.24$ both flame shapes can be observed. After the change in flame shape, further increasing $\mathcal{P}_{H_2}$ leads to a progressive reduction of L_f. At $\mathcal{P}_{H_2} = 0.27$ the system becomes unstable and a limit cycle is established. Further increasing the hydrogen content from $\mathcal{P}_{H_2} = 0.27$ pushes the system to a higher amplitude limit cycle.

The transition from a stable state into a limit cycle is also shown in Fig. 3 by spectrograms of pressure p_1' and heat release rate Q'. The rms of the heat release rate (Q_{rms}') and pressure ($p_{1\text{rms}}'$) time series, proportional to the total energy of each spectra are shown to the right of the figure. For $\mathcal{P}_{H_2} < 0.26$ the total energy of the fluctuations is very low and hence the combustor is deemed stable. However, there are traces of energy peaks at frequencies corresponding to acoustic modes of the combustor at $f \approx 785$ Hz and $f \approx 1113$ Hz, which may be an indica-
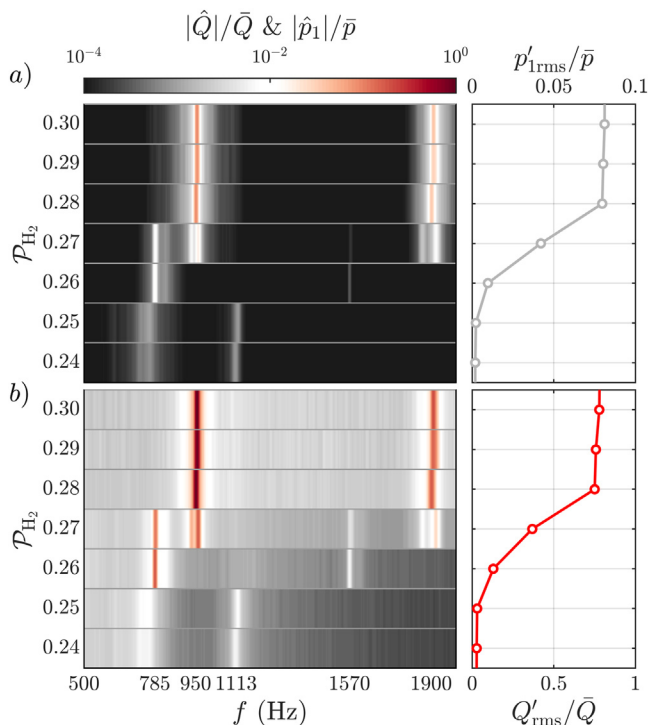
Fig. 3. Spectrograms of p'_1 and $Q'/\bar{Q}$ at different power fractions $\mathcal{P}_{H_2}$.

tion of intermittency [39]. As hydrogen content is increased to $\mathcal{P}_{H_2} = 0.27$ a stable limit cycle establishes with a frequency $f \approx 785$ Hz and amplitudes $Q'_{rms}/\bar{Q} = 0.12$ and $p'_{1rms}/\bar{p} = 0.01$, where $\bar{p}$ is the atmospheric pressure. By increasing the hydrogen content to $\mathcal{P}_{H_2} > 0.28$, the frequency switches to $f \approx 950$ Hz and the amplitude of the oscillations increases considerably to $Q'_{rms}/\bar{Q} = 0.73$ and $p'_{1rms}/\bar{p} = 0.08$.

Since the thermal power P and the equivalence ratio ϕ are held constant, an increase in hydrogen content leads to a very small change in the bulk velocity, hence, it is approximately constant (see Table 1). Therefore, the observed changes in the flame shape and the establishment of a limit cycle are only due to the change in the mixture fraction of the fuel.

4. Flame length characterization

Since the changes in the flame shape are only due to the variation in hydrogen content, we can directly associate any changes in the flame length L_f to the changes in $\mathcal{P}_{H_2}$. Fig 4 shows the mean flame shapes from experimental set B using the shorter combustion chamber ($L_q = 80$ mm) which allows us to reach higher values of hydrogen content without triggering any instabilities. The flame shapes and lengths in this figure display a similar pattern to that described in the previous section. Fig 5 shows a plot of the values of L_f as a function of $\mathcal{P}_{H_2}$ using the two different combustor lengths. The squared white markers correspond to the measurements from Fig. 2 and the round black markers to Fig. 4. Note that L_f does not change significantly with the different combustor lengths; the variation is less than 3%[1]. For both combustor lengths the general trend is the same, L_f reduces as hydrogen content increases, except for the region $0.19 < \mathcal{P}_{H_2} < 0.24$ shaded in gray. This corresponds to the bi-stable region where both flame shapes can be observed. In this region the flame can spontaneously switch

---

[1] The variation is estimated from statistical analysis of the difference between L_f obtained using $L_q = 80$ mm and L_f obtained using $L_q = 150$ mm.

from one shape to the other. Depending on the observed flame shape, we obtain a different value of the flame length. Hence in the bi-stable region L_f can change abruptly. To investigate if this region is linked to the flame speed and not necessarily to the hydrogen concentration, the flame speed was reduced by lowering the equivalence ratio to $\phi = 0.6$ at $\mathcal{P}_{H_2} = 0.3$ (experimental point C in Section 2.2). Under these conditions, the same switching phenomena is observed. This indicates that the switching occurs at some operating conditions where the flame shape is very sensitive to the flame speed. It should be emphasized that this phenomena is highly geometry dependent. However, a similar effect may be expected to occur in other configurations.

To model the change in L_f as a function of hydrogen content, the laminar flame speed S_L is computed for the range of $\mathcal{P}_{H_2}$ values using Cantera [40]. In Fig. 5, the curve K_1/S_L corresponding to the detached flame model is shown with a black line, and the curve K_2/S_L corresponding to the attached flame model is shown with a red line. Here K_1 and K_2 are proportionality constants and the shaded regions surrounding these curves correspond to $\pm 3\%$ of the mean value. For these flames it can be seen that a decrease in L_f closely follows an increase in laminar flame speed. Thus the evolution of the flame speed, as a function of hydrogen content can be used as a model for the characteristic flame length. Then, the characteristic flame length model can be used, in turn, as an input for the flame transfer function.

5. Flame transfer function

To predict the influence of hydrogen in combustion instabilities it is instructive to begin by analysing the influence of hydrogen on the flame transfer function (FTF). The FTF relates the response of the unsteady rate of heat release to the velocity fluctuations measured at a reference position, which in this case corresponds to the dump plane at $z = 0$:

$$\text{FTF}(\omega) = \frac{\hat{Q}/\bar{Q}}{\hat{u}/\bar{u}}. \tag{2}$$

The hatted quantities denote the Fourier transform at frequency $\omega = 2\pi f$. Fig 6 shows measured FTFs using the shorter combustion chamber ($L_q = 80$ mm) and the convention $\text{FTF} = Ge^{i\theta}$, where G is the gain, and θ the phase. The FTFs were obtained using a forcing level of 5% and they correspond to the mean flame shapes shown in Fig. 4. Two important features of the FTFs with increasing hydrogen content are the increase in the cut-off frequency and shortening of the time delay. On the one hand, the higher cut-off frequencies can promote the appearance of peaks and troughs in the gain and phase of the FTF, if convective-acoustic disturbances are generated by the geometry [21–23]. This phenomenon has been observed, for instance, in many swirled configurations [41–44]. On the other hand, the shortening of the time delay with increasing hydrogen content, which corresponds to the reduction in the slope of the phase θ, has also been observed in laminar slit flames [26] and is closely linked to the laminar flame speed.

The FTF is very sensitive to the flame shape, hence care must be taken when measuring in the bi-stable region. To demonstrate this, the FTF of experimental point C ($P = 7$ kW, $\phi = 0.6$, $\mathcal{P}_{H_2} = 0.3$, $L_q = 80$ mm) is measured and shown in Fig. 7. At this condition, the flame changes shape at different forcing frequencies. The red squared markers correspond to the FTF measurements where the flame is attached to the wall, and the black round markers to the detached flame. The insets show one flame image for each case. In this figure we observe that the gain and phase of the FTF can change abruptly depending on the observed flame shape.

Fig 8 shows the stream-wise distribution of the heat release rate for each of these flame shapes. As shown before, this figure reaffirms that the detached flame has a longer characteristic
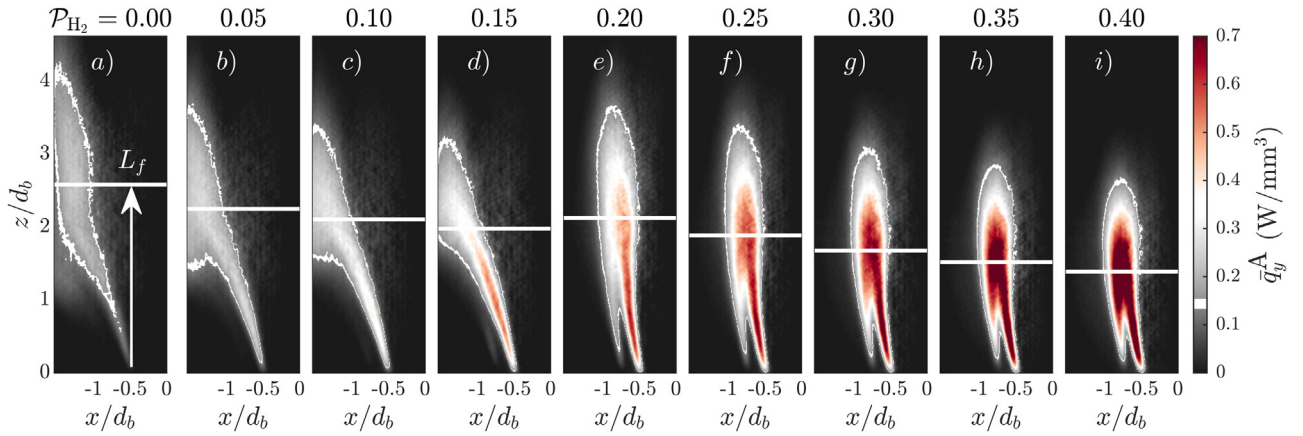
Fig. 4. Abel deconvoluted mean flame images $\bar{q}_y^A$ shown for $x/d_b < 0$ corresponding to experimental set B. Operating conditions: $P = 7$ kW, $\phi = 0.7$, $L_q = 80$ mm, and increasing hydrogen content $\mathcal{P}_{H_2}$.
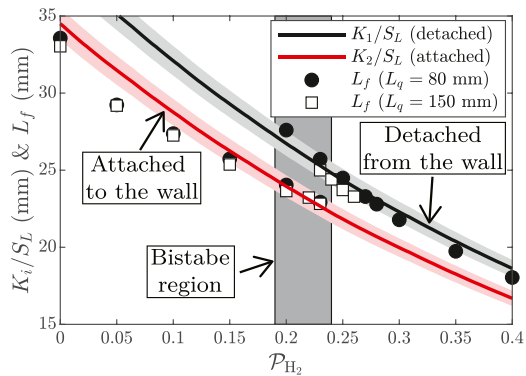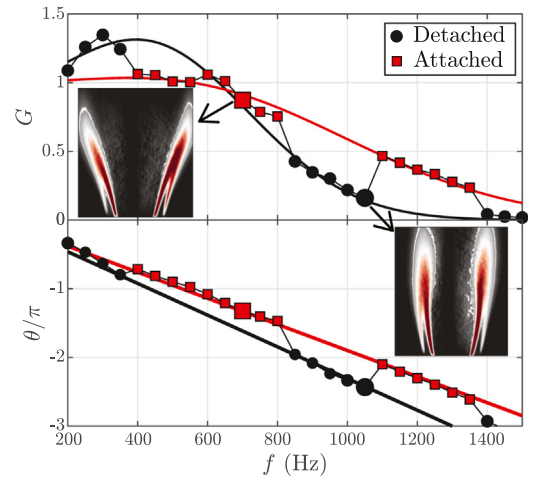

Fig. 5. Characteristic flame length L_f vs hydrogen content. The markers show the experimental values of L_f with the two quartz lengths. The gray shaded area shows the region where both attached and detached flames are observed. The curves correspond to K_i/S_L, where $K_1 = 7.40 \times 10^{-3}$ m^2/s and $K_2 = 6.64 \times 10^{-3}$ m^2/s. The shaded areas surrounding these curves correspond to $\pm 3\%$ of the mean value.
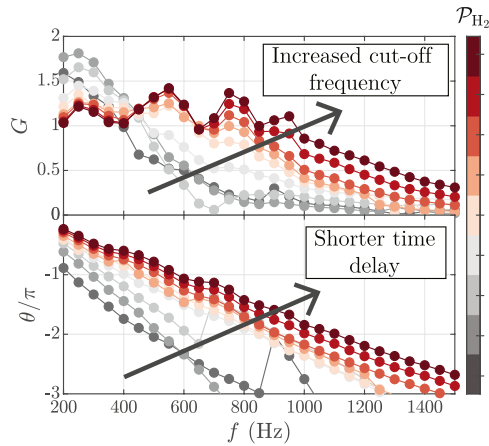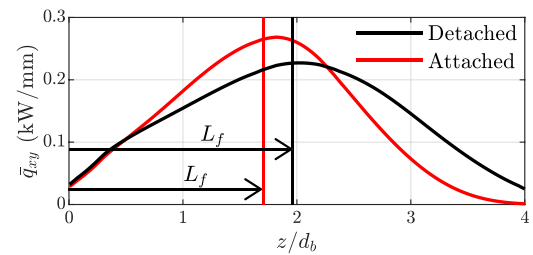

Fig. 6. Experimental flame transfer functions as a function of frequency and hydrogen content.

Fig. 7. Flame transfer function measured in the bi-stable region with both flame shapes present (experimental point C). Operating conditions: $P = 7$ kW, $\phi = 0.6$, $\mathcal{P}_{H_2} = 0.3$, $L_q = 80$ mm.

Fig. 8. Stream wise distribution of heat release rate for both flame shapes and corresponding flame lengths L_f (experimental point C). Operating conditions: $P = 7$ kW, $\phi = 0.6$, $\mathcal{P}_{H_2} = 0.3$, $L_q = 80$ mm.

flame length L_f in the bi-stable region. Furthermore, by rescaling the FTF from Fig. 7 by $L_f/\bar{u}$, as done in Fig. 9, one observes that phases align in the same slope. This shows that $\tau = L_f/\bar{u}$ is the relevant time scale for these FTFs regardless of the flame shape.

For flames that are attached to the bluff-body ($\mathcal{P}_{H_2} \geq 0.15$), Æsøy et al. [21] proposed a model for the FTFs based on two dis-

tributions of time lags (DTL) of the form:

$$\text{FTF}(\omega, L_f, \bar{u}) = \text{DTL}_1 + \text{DTL}_2, \tag{3}$$

where

$$\text{DTL}_j(\omega) = \frac{g_j}{2}\left(e^{-\frac{1}{2}(\omega+\beta_j)^2\sigma_j^2} + e^{-\frac{1}{2}(\omega-\beta_j)^2\sigma_j^2}\right)e^{-i\omega\tau_j}, \tag{4}$$

and the parameters g_j, β_j, σ_j, τ_j are functions of the characteristic length L_f and the bulk velocity at the dump plane $\bar{u}$. Details of the FTF parameters' dependence on L_f and $\bar{u}$ are given in Appendix A. The reconstructed flame transfer functions are shown in Fig. A.19 for different values of $\mathcal{P}_{H_2}$. The reconstruction success-
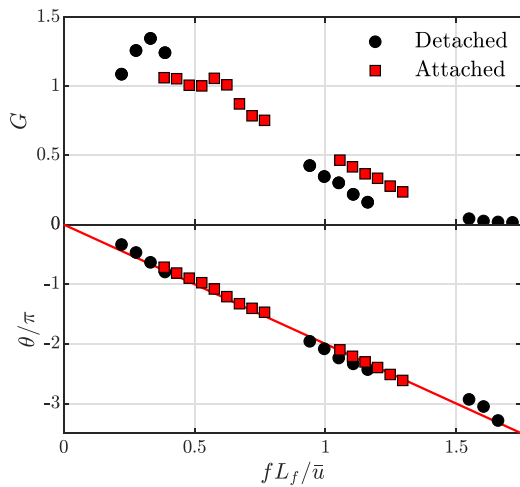
Fig. 9. Flame transfer functions scaled by $L_f/\bar{u}$. Operating conditions: $P = 7$ kW, $\phi = 0.6$, $\mathcal{P}_{H_2} = 0.3$, $L_q = 80$ mm.

Fig. 10. Trajectories of the eigenvalues as $\mathcal{P}_{H_2}$ is increased. The gray shaded area is the unstable half plane. Results for the detached flame length model $L_f = K_1/S_L$.

fully captures the peaks and troughs in the gain and the phase, the low pass filter structure, the shift in the time delay and the increase in cut off frequency. Notice that this comparison was only performed to validate the model's ability to reproduce the FTFs. For the linear stability analysis presented in the following section, only L_f obtained from the mean flame images and $\bar{u}$ are required.

6. Stability analysis

6.1. Modelling approach

For design purposes, it is desirable to predict the limit of stability as hydrogen is introduced into the system, as well as the different features of the limit cycles. To do this we use a low order thermoacoustic network model that considers a mean flow and semi-perfect gas properties. At a glance, the modelling approach is a network of ducts where 1D acoustic waves propagate. The ducts are joined by acoustically compact jump conditions which emulate area changes or heat sources. The jump conditions relate the properties from one duct to the other by applying quasi-steady conservation laws for mass, momentum and energy as given in Dowling and Stow [32]. The network model is completed by prescribing boundary conditions at the inlet and outlet of the configuration.

The inlet boundary condition is modelled using a reflection coefficient $R_i = 0.90$ chosen to match the impedance measured experimentally. The outlet boundary condition is modelled using an open end, $\hat{p} = 0$. The flame is located at a distance L_f from the dump plane and it is modelled using Eq. (3), where the reference point for the velocity fluctuations is taken to be just before the combustion chamber. As far as this modelling approach is concerned, adding hydrogen has two effects:

1. Changing the flame transfer function (FTF), as discussed in the previous section.
2. Changing the thermodynamic properties of the gas mixture.

The latter, however, is negligible compared to the effect imposed by changing the FTF in the current configuration. For the present configuration the network model is shown in Fig. 17.

6.2. Linear stability as a function of hydrogen content

To assess the linear stability we compute the eigenvalues of the system as a function of hydrogen content. The eigenvalues are decomposed as $\omega = 2\pi f - i\lambda$, where λ is the growth rate. Using the
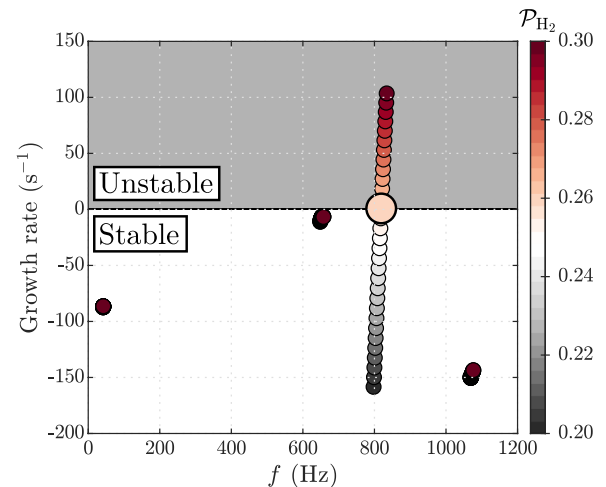
network model we compute the trajectories of the eigenvalues in the complex plane. More specifically, we track the growth rate as $\mathcal{P}_{H_2}$ is increased. The results are shown first for K_1/S_L in Fig. 10, corresponding to the trajectory of the detached flame shape.

When $\mathcal{P}_{H_2} = 0.20$ the model predicts 4 resonant modes with $f \approx 42$ Hz, 649, 802, 1068 Hz. The frequencies of the last two modes, are very close to those observed in the spectrogram (Fig. 3) when $\mathcal{P}_{H_2} < 0.27$. As the hydrogen content is increased, the mode at 802 Hz becomes unstable, consistent with experimental observations. The model predicts the stability limit to be at $\mathcal{P}_{H_2} \approx 0.268 \pm 0.020$, matching the experimental value at $\mathcal{P}_{H_2} = 0.27$. The growth rate of the mode at 802 Hz increases with hydrogen content, meaning that as $\mathcal{P}_{H_2}$ increases the system saturates faster into a limit cycle. The accuracy of this prediction is owed to the ability of the FTF model to capture the evolution of the flame response as the amount of hydrogen in the fuel mixture is varied. Finally, we note that the frequency of oscillation increases with hydrogen content, as previously reported by Zhang and Ratner [45].

6.3. Linear stability of the two flame models

The same process is repeated for the attached flame length model (K_2/S_L) and the two trajectories of the unstable eigenvalue around 802 Hz are shown in Fig. 11a. Note that the vertical axis has been flipped upside down for visualization purposes. The red line shows the evolution of the growth rate for the attached flame length model. The red shaded region corresponds to the variation in growth rate due to a $\pm 3\%$ variation in the flame length. Notice that this small variation translates to $\approx \pm 50$ s^{-1} change in the growth rate due to the high sensitivity of thermoacoustic systems [46]. Similarly, the black line and gray shaded region correspond to the growth rate obtained using the detached flame length model, which was already shown in Fig. 10. Fig. 11b shows the corresponding flame length models and experimental data points.

Starting from the attached flame length model (red line) at $\mathcal{P}_{H_2} = 0.15$, the linear stability analysis predicts that the system is stable. In experiments we observe the flame attached to the combustor wall. Progressively increasing hydrogen content reduces the growth rate and the flame length until they reach the neutral stability line at $\mathcal{P}_{H_2} = 0.199$ and $\mathcal{P}_{H_2} = 0.229$, respectively. At this point instead of saturating into a limit cycle oscillation, the flame changes shape as indicated by the arrows A in Fig. 11a and B in Fig. 11b. The change in flame shape results in an elongated flame detached from the wall (black line) with a larger value of L_f that
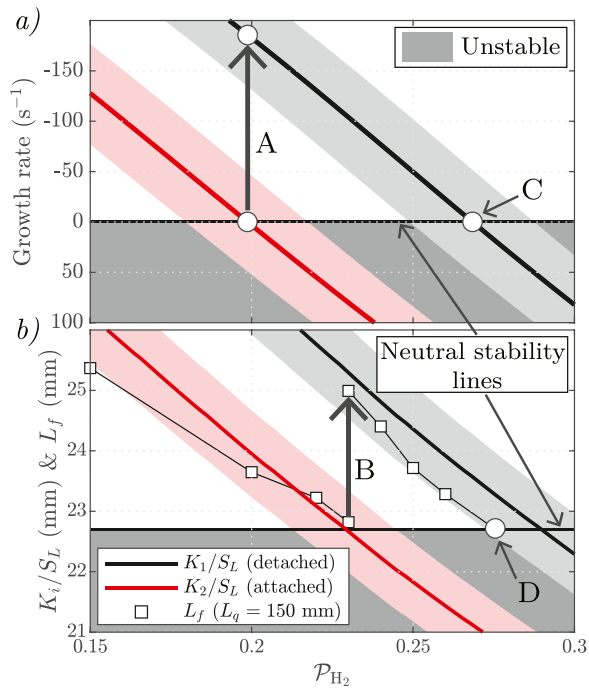
Fig. 11. (a) Growth rate vs $\mathcal{P}_{H_2}$ of the mode around 802 Hz, using the two different models for the characteristic flame length. The shaded areas surrounding the curves correspond to the variation in growth rate due to the ±3% variation in the flame length. The vertical axis has been flipped upside down. (b) Zoom in of Fig. 5 to the region where the flame changes shape using $L_q = 150$ mm. The dark gray shaded regions correspond to the unstable plane.

pushes the system to the stable half plane. After this transition any further increase in hydrogen content reduces the growth rate and the flame length until the system becomes unstable at $\mathcal{P}_{H_2} = 0.27$ (points C and D in Fig. 11).

In summary, the linear stability analysis using a scaled FTF model which is a function of the hydrogen content, is able to predict the onset of instability as the operating conditions are varied. For this geometry, the FTF model also predicts that the wall attached flames become unstable faster than the detached flames due to shorter flame lengths, consistent with the transition observed in experiments. This analysis shows that the main effect of hydrogen is to reduce the flame length L_f leading to the onset of an instability which is well captured using established modeling tools (acoustic network models). It is also demonstrates that if L_f can be linked to the operating conditions, then the FTF can be potentially modelled using the scaling approach of Æsøy et al. [21], where only measurements of the mean flame and bulk velocity are needed. This methodology has the potential of reducing the amount of measurements/simulations needed to describe the FTF and thus, the speeding up the linear stability analysis significantly.

7. Nonlinear analysis

In the previous section we examined the consequences of the flame shape transition and the onset of the instability as hydrogen content is increased using a linear framework. In this section we will study the characteristics of the limit cycle at an operating point near the onset of instability.

To get more insight into the dynamics of the low and high saturation amplitudes of the limit cycle oscillation we begin by analysing the time series of p_1' and Q' at $\mathcal{P}_{H_2} = 0.28$ as shown in Fig. 12. The low amplitude limit cycle at $f = 785$ Hz persists for
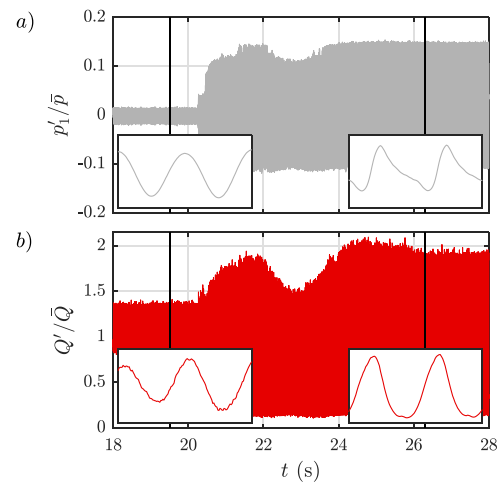
Fig. 12. (a) Time series of p_1' and (b) time series of $Q'/\bar{Q}$ at $\mathcal{P}_{H_2} = 0.28$ where the limit cycle switches from $f = 785$ Hz to $f = 950$ Hz. The insets show zoom in regions near the black vertical lines highlighting the waveform of p_1' and Q'.

about 20 s before it experiences a rapid transition[2] to a higher amplitude and higher frequency $f = 950$ Hz. The insets show zoomed in regions at the times $t = 19.5$s and $t = 26.5$s corresponding to the vertical black lines. This is before and after the transition. Before the transition, both pressure and heat release rate fluctuations are approximately monochromatic. After the transition, both signals show the presence of harmonics. The first of these additional harmonics can be seen in the spectrograms of Fig. 3 at $f = 1900$Hz.

7.1. Rayleigh criterion

To understand the strength of the limit cycle it is helpful to analyse the phase difference between pressure and unsteady heat release rate, as per the Rayleigh criterion. The multiple microphone method (MMM) [47] is used to reconstruct the pressure $\hat{p}$ and velocity $\hat{u}$ at the dump plane. Then, the phase difference between pressure and unsteady heat release rate $\angle(\hat{p}/\hat{Q})$ is computed and shown in Fig. 13b.

During the low amplitude limit cycle, the phase between the pressure and the unsteady heat release rate is $\angle(\hat{p}/\hat{Q})/\pi = -0.25$. Therefore, the flame is feeding some energy into the acoustics of the system. As the mode switches to the high amplitude limit cycle at $f = 950$Hz the phase difference becomes zero, meaning that all the unsteady energy released by the flame is being fed to the acoustics of the system, thus explaining the high levels of pressure fluctuations.

This change leads to a significant increase in the acoustic velocity $|\hat{u}|/\bar{u}$ which is shown in Fig. 13a. Before the transition $|\hat{u}|/\bar{u} = 0.23$ and $|\hat{Q}|/\bar{Q} = 0.17$. After the transition $|\hat{u}|/\bar{u}$ increases to 2.63 indicating reversed flow in parts of the cycle at the dump plane. This implies that the flame is periodically flashing back upstream of the bluff body leading to $|\hat{Q}|/\bar{Q} = 0.97$.

The phase averaged unsteady heat release rate is shown in Fig. 14 where (a) shows the cycle for $t < 20$s and (b) for $t > 20$s. Before the transition, the flame is still stabilized as an 'M-flame', where the cyclic variation of unsteady heat release rate is caused by vortex roll-up. The roll-up process leads to an increase of unsteady heat release rate as seen from $t/T = [0.1$ to $0.7]$. Here $t/T = 0$ and $t/T = 0.5$ correspond respectively to the minimum and

---

[2] The 20 seconds mark varies between experimental runs, however the transition from the low amplitude limit cycle at $f = 785$Hz to the high amplitude one at $f = 950$Hz is always observed.
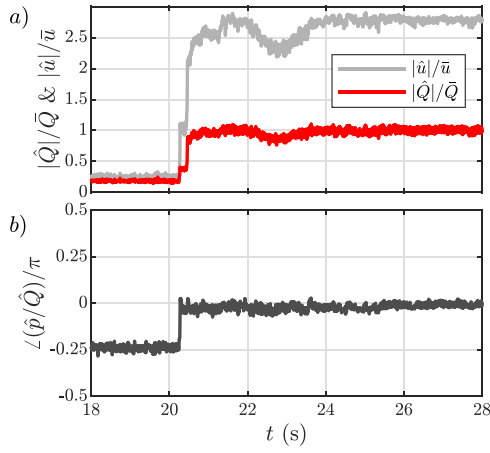
Fig. 13. (a) Time series of the magnitude of the acoustic velocity $|\hat{u}|/\bar{u}$, and the heat release rate fluctuations $|\hat{Q}|/\bar{Q}$. (b) Phase difference $\angle(\hat{p}/\hat{Q})/\pi$.

maximum fluctuation of the global HRR. Between $t/T = 0.7$ and $t/T = 0.0$, the vortex pinches off leading to annihilation of flame surface. During the entire cycle, the flame is well stabilized on the inner and outer lips of the bluff body at the dump plane. For the strong limit cycle, $t > 20s$ shown in (b) the case changes significantly. Due to the strong velocity fluctuations the flow reverses for part of the cycle. As seen from $t/T = [0.8$ to $0.0]$ the flame flashes back into the injector pipe. This is confirmed by images of the bluff body glowing red, see Fig. 14d and compare it to Fig. 14c. From $t/T = [0.1$ to $0.2]$ the flame reattaches to the bluff body and begins to propagate downstream. Between $t/T = [0.3$ to $0.7]$ the flame surface area grows driven by the velocity fluctuations and then the cycle restarts.

### 7.2. Describing function analysis

To characterize the features of the limit cycle oscillations in the model, we require a flame describing function (FDF). Fig 15 shows the measured FDF at different forcing amplitudes, $A = |\hat{u}|/\bar{u}$, and at the operating conditions in which the limit cycle is observed. First, we can observe that the gain features a hump, where the gain first increases, then decays, and finally it remains constant up to the
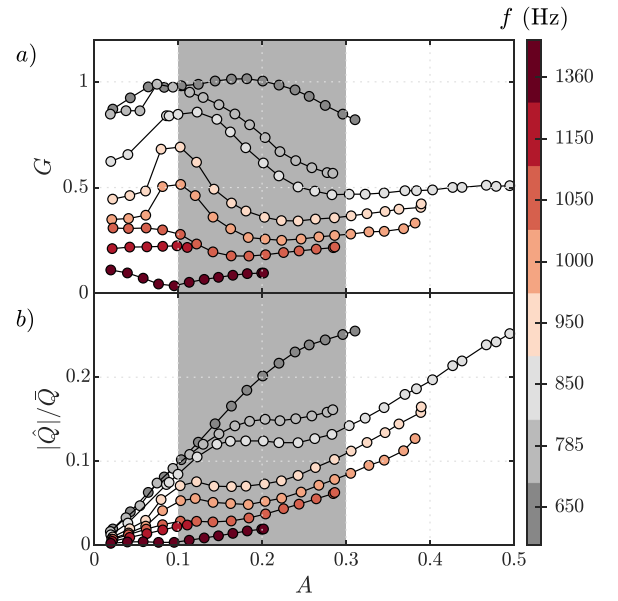
Fig. 15. (a) FDF and (b) normalised unsteady heat release rate as a function of the forcing amplitude A. The operating conditions are at $\phi = 0.7$, $P = 7$ kW and $\mathcal{P}_{H_2} = 0.27$. The gray shaded region corresponds to the regions where partial saturation of the heat release rate is observed.

point where the measurements were taken. The decay observed in the gain at amplitudes $0.1 < A < 0.3$ (gray shaded region), which corresponds to the horizontal flattening of $|\hat{Q}|/\bar{Q}$ in Fig. 15b, is therefore only due to a partial saturation of the heat release rate. This is a key observation when trying to estimate the amplitude of the limit cycle, because as seen in Fig. 13, the heat release first saturates to an amplitude of about $|\hat{Q}|/\bar{Q} = 0.17$ and then grows to $|\hat{Q}|/\bar{Q} \approx 0.97$. Therefore the partial saturation of the heat release rate in the region $0.1 < A < 0.3$ should explain the presence of the first limit cycle. We expect that at much higher amplitudes $|\hat{Q}|/\bar{Q} \to 1$ indicating full saturation and which would correspond to the stronger limit cycle.

In the network model the FDF is implemented by fitting the available data to a single distribution of the form shown in Eq. (4). In the linear regime we observed that only the mode at $f \approx 802$ Hz
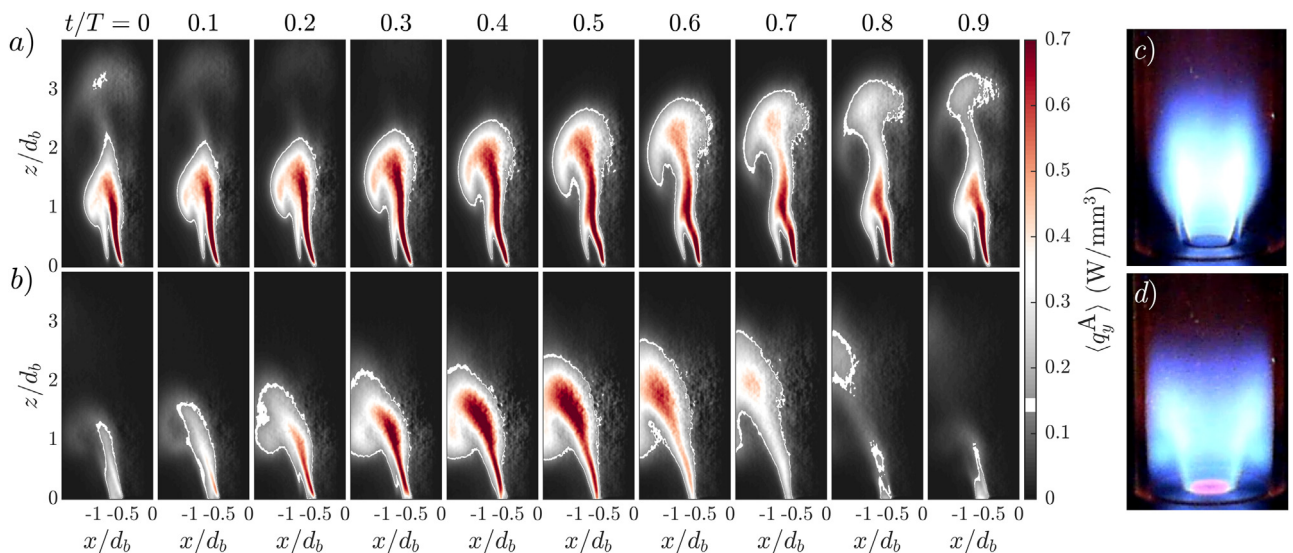
Fig. 14. Phase averaged unsteady heat release rate $\langle q_y^A \rangle$ shown through one cycle for (a) $t < 20$ s in Fig. 13 and for (b) $t > 26$ s. (c) and (d) show corresponding snapshots of the flame and bluff body.
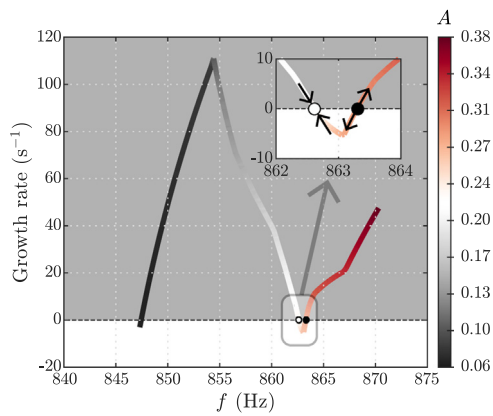
Fig. 16. Trajectory of the unstable eigenvalue as a function of the forcing amplitude A. The operating conditions are at $\phi = 0.7$, $P = 7$ kW and $\mathcal{P}_{H_2} = 0.27$.

becomes unstable when the hydrogen content is increased. In the nonlinear regime we track this mode as the amplitude is increased as shown in Fig. 16. The first observation is that the frequency of the mode at low amplitudes, differs from that of the linear analysis. This is due to the lower resolution of the FDF, which was evaluated at considerably less frequencies than the FTFs. The growth rate of the mode as a function of amplitude shows a pattern similar to an "N". It first increases, reaching a maximum around of $\lambda = 111$ s^{-1} at $A = 0.10$, then it decays crossing the zero growth rate line at $A \approx 0.23$. It further decreases to a minimum of $\lambda = -5$ s^{-1} at $A = 0.28$ and finally it increases again. This reveals the existence of a neighbouring unstable limit cycle with amplitude $A \approx 0.30$.

Save for the frequency, these tendencies match experimental observations very accurately. The model predicts that the amplitude first grows and saturates at $A \approx 0.23$, when the growth rate becomes zero for the first time. This corresponds to the partial saturation of the heat release rate observed in Fig. 15. The mode shapes computed at this amplitude and a comparison with the experimental measurements are shown in Fig. 17. After the partial saturation is reached, the neighbouring unstable limit cycle allows the system to trigger. Thus the system can reach higher unstable amplitudes that promote growth until full saturation is reached at a much higher amplitude. Unfortunately due to the capabilities of the experimental forcing we do not have data beyond $A = 0.38$,

and thus we can not compute the strong limit cycle. However, Fig. 16 suggests that as the amplitude increases, so does the frequency. This could explain the frequency of 950 Hz observed in strong limit cycle.

While the FDF can be used to describe the experimental observations, it was only measured at a single operating condition. Therefore it is left for future studies to determine if the observed limit cycle behavior, the features of the FDF, and triggering to the high amplitude limit cycle are a function of hydrogen content.

8. Conclusion

An experimental investigation of the effects of hydrogen content on the stability of a laboratory scale combustor is carried out. The hydrogen content, here expressed in terms of power fraction $\mathcal{P}_{H_2}$ is used as a bifurcation parameter. When $\mathcal{P}_{H_2} = 0$ the methane flame is lifted and detached from the wall. As $\mathcal{P}_{H_2}$ increases the flame shortens and attaches to the bluff body. A further increase in hydrogen content makes the flame change shape and detach from the wall. When $\mathcal{P}_{H_2} = 0.27$ a limit cycle is established.

A reduced order model consisting of a network of acoustic elements and a flame transfer function (or a flame describing function) is used to predict the stability of the system. The model for the flame transfer function receives as input parameters the flame length and the bulk velocity at the dump plane. The flame length, computed as the downstream centre of intensity, is therefore characterized as a function of hydrogen content. It is observed that the flame length is proportional to the inverse of the flame speed and depending on the observed flame shape, the proportionality constant changes. The linear stability analysis is carried out using two flame length models, one for the flame attached to the combustor wall and one for the detached flame. The results show that the flame shape transition occurs when the model using the flame attached to the combustor wall becomes unstable. The model is also able to accurately capture the bifurcation point and the properties of the limit cycle.

This study shows that the flame shape transition observed occurs so as to keep the system from becoming unstable. Furthermore, it also validates the use of the flame transfer function together with a network model and shows that premixed hydrogen can be safely analyzed with the same tools as regular hydrocarbons. However, special attention is required to model the influence of hydrogen in both the characteristic flame length and the flame
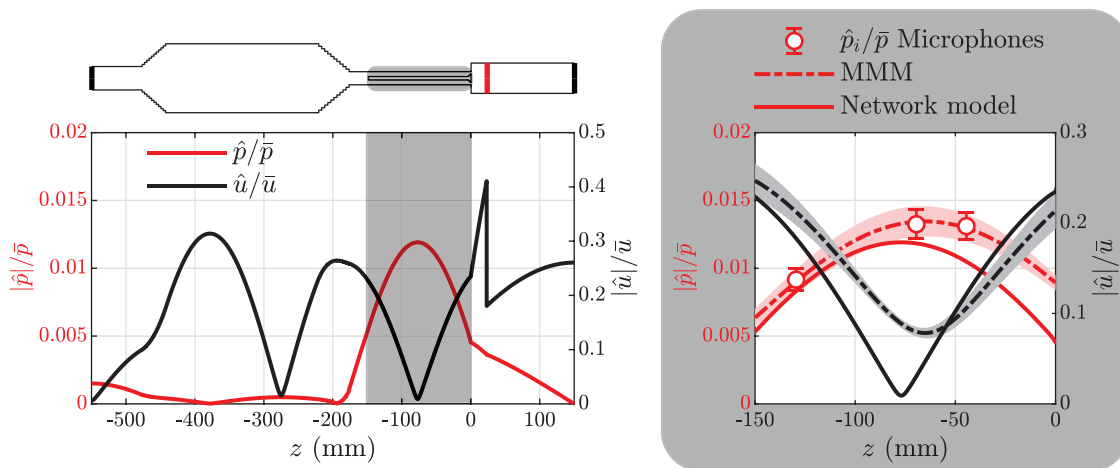
Fig. 17. Network model and mode shapes. The network model is shown in the top left corner. The gray shaded areas correspond to the region inside the injection pipe where pressure measurements are taken in the experimental set up. The plot on the left shows the normalized pressure and velocity mode shapes at limit cycle conditions as a function of z, computed with the network model. On the right we show an inset to the injector pipe region and compare the mode shapes from the MMM and the network model. The main difference in mode shapes is due to the predicted frequency of the nonlinear model.

transfer function. This is due to the fact that as hydrogen content increases and the flame shortens, geometric effects such as wall interactions may be removed and these have a direct influence in the shape of the flame and its properties. In general, the predicting capabilities of the models used in this study are owed to their ability to capture the flame response as the operating conditions, including hydrogen content, are varied.

Declaration of Competing Interest

The authors declare that they have no known competing financial interests or personal relationships that could have appeared to influence the work reported in this paper.

Acknowledgments

Appendix A. Calculation of FTF parameters.

The flame transfer function as a function of the operating conditions is given by:

$$\text{FTF}(\omega, L_f, \bar{u}) = \text{DTL}_1 + \text{DTL}_2. \tag{A.1}$$

where

$$\text{DTL}_j(\omega) = \frac{g_j}{2}\left(e^{-\frac{1}{2}(\omega+\beta_j)^2\sigma_j^2} + e^{-\frac{1}{2}(\omega-\beta_j)^2\sigma_j^2}\right)e^{-i\omega\tau_j}, \tag{A.2}$$

To compute the parameters of the FTF (g_j, β_j, σ_j, τ_j for $j = 1, 2$) we begin by linking the characteristic flame length to the hydrogen content via:

$$L_f(\mathcal{P}_{H_2}) = \frac{K_i}{S_L(\mathcal{P}_{H_2})}, \tag{A.3}$$

where S_L is the laminar flame speed computed with Cantera, which is a function of $\mathcal{P}_{H_2}$, and K_i is a constant of proportionality. The curves for S_L are shown in Fig. 5. For the attached flame model we

have $K_1 = 7.40 \times 10^{-3}$ m$^2/s$ and for the detached flame model we have $K_2 = 6.64 \times 10^{-3}$ m$^2/s$. Then, using the method proposed in Æsøy et al. [21] we begin by defining the cut-off frequency of the FTF as:

$$\omega_c = 2\pi c_1 \frac{\bar{u}}{L_f} \tag{A.4}$$

The parameters of the first distribution are given by:

$$\tau_1 = \frac{L_f}{\bar{u}}, \tag{A.5}$$

$$\beta_1 = \frac{\omega_c}{1 + c_2\sqrt{\log(2)}}, \tag{A.6}$$

$$\sigma_1 = \frac{1}{c_2\beta_1}, \tag{A.7}$$

For the second distribution we have:

$$g_2 = c_3, \tag{A.8}$$

$$\tau_2 = \tau_1 + \frac{L_g}{\bar{u}_p}, \tag{A.9}$$

$$\beta_2 = 2\pi c_4 \frac{\bar{u}_p}{d_g}, \tag{A.10}$$

$$\sigma_2 = \frac{1}{c_5\beta_2}, \tag{A.11}$$

where $L_g = 45$ mm is the distance of the grub screws from the dump plane, $\bar{u}_p \approx 0.57\bar{u}$ is the flow velocity in the injector pipe and $d_g = 4$ mm is the grub screw diameter. By requiring that FTF $\to 1$ as $\omega \to 0$, [48], we obtain the value of g_1:

$$g_1 = \exp\left(\frac{1}{2}\beta_1^2\sigma_1^2\right)\left(1 - g_2\exp\left(-\frac{1}{2}\beta_2^2\sigma_2^2\right)\right). \tag{A.12}$$
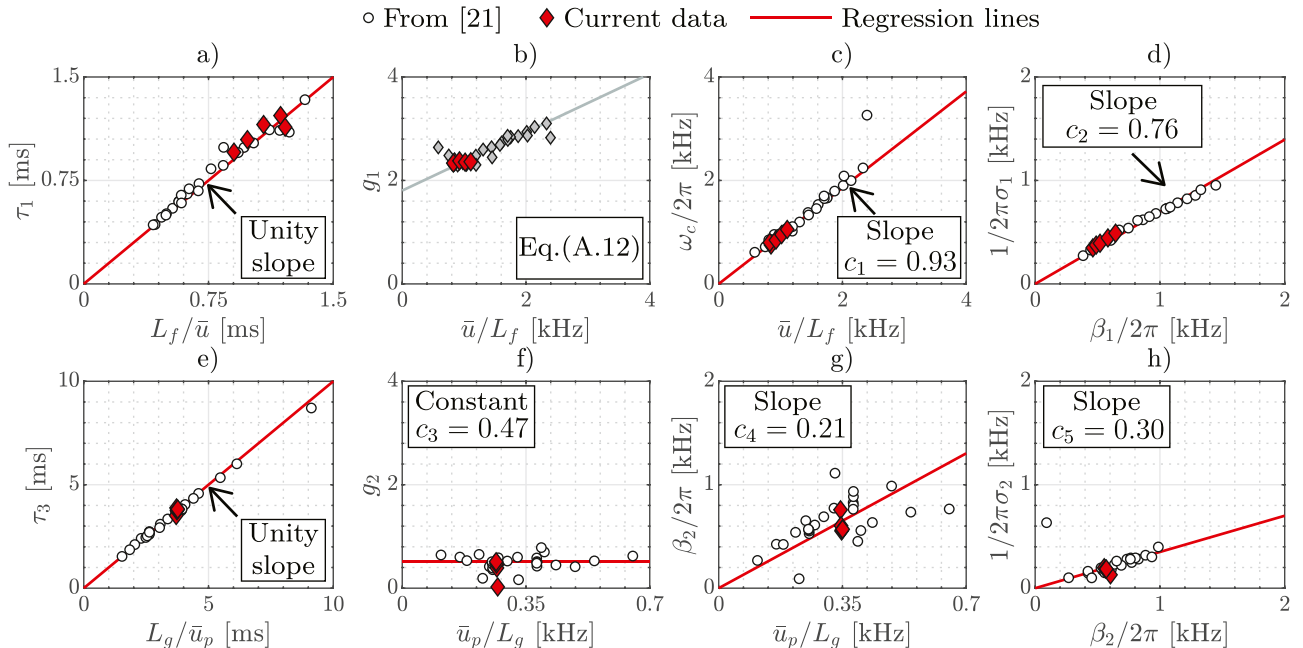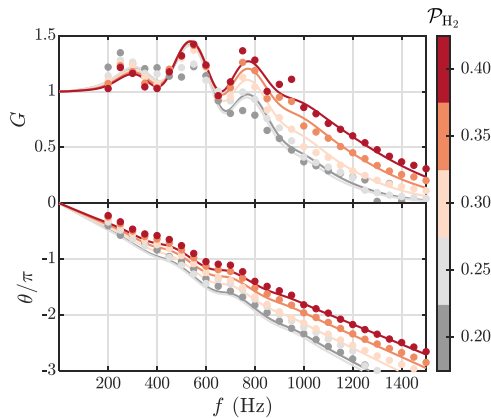

Fig. A1. Scaling of FTF parameters with operating conditions (adapted from [21]). The red markers indicate the operating conditions considered in this study. Fig. A1e) shows $\tau_3 = L_g/\bar{u}_p = \tau_2 - \tau_1$.

Table A1

Fitting constants for the FTF.

Constant	Value	Constant	Value
c_1	0.9342	c_4	0.2063
c_2	0.7601	c_5	0.2956
c_3	0.4718		

Fig. A2. Experimental (round markers) and reconstructed flame transfer functions at $\phi = 0.7$, $P = 7$ kW and increasing hydrogen content.

The values of the fitting constants $c_1, c_2, \ldots, c_5$ are given in Table A.2, and the reader is referred to [21] for their physical interpretation.

Fig A1, shows values of the FTF parameters as a function of the operating conditions. This figure shows with red markers the data from this paper overlaid on top of the data from Æsøy et al. [21] (white markers). The red lines show the trends used to compute the fitting constants. Reconstructed flame transfer functions are shown in Fig. A.19, where one can clearly observe that the main trends, such as increased cut-off frequency and shortening of the time delay, are accurately captured by the model.

Supplementary material

Supplementary material associated with this article can be found, in the online version, at doi:10.1016/j.combustflame.2022. 112323

References

[1] G. Koroll, R. Kumar, E. Bowles, Burning velocities of hydrogen-air mixtures, Combust. Flame 94 (3) (1993) 330–340, doi:10.1016/0010-2180(93)90078-h.

[2] T. Boushaki, Y. Dhué, L. Selle, B. Ferret, T. Poinsot, Effects of hydrogen and steam addition on laminar burning velocity of methane–air premixed flame: experimental and numerical analysis, Int. J. Hydrog. Energy 37 (11) (2012) 9412–9422, doi:10.1016/j.ijhydene.2012.03.037.

[3] D. Beerer, V. Mcdonell, P. Therkelsen, R.K. Cheng, Flashback and turbulent flame speed measurements in hydrogen/methane flames stabilized by a low-swirl injector at elevated pressures and temperatures, J. Eng. Gas Turbine Power 136 (3) (2013), doi:10.1115/1.4025636.

[4] P. Chiesa, G. Lozza, L. Mazzocchi, Using hydrogen as gas turbine fuel, J. Eng. Gas Turbine Power 127 (1) (2005) 73–80, doi:10.1115/1.1787513.

[5] M.R. Bothien, A. Ciani, J.P. Wood, G. Fruechtel, Toward decarbonized power generation with gas turbines by using sequential combustion for burning hydrogen, J. Eng. Gas Turbine Power 141 (12) (2019), doi:10.1115/1.4045256.

[6] European Turbine Network, Hydrogen and gas turbines: the path towards a zero-carbon gas turbine, ETN Global, 2020. Technical Report

[7] J. Beita, M. Talibi, S. Sadasivuni, R. Balachandran, Thermoacoustic instability considerations for high hydrogen combustion in lean premixed gas turbine combustors: a review, Hydrogen 2 (1) (2021) 33–57, doi:10.3390/hydrogen2010003.

[8] G. Oztarlik, L. Selle, T. Poinsot, T. Schuller, Suppression of instabilities of swirled premixed flames with minimal secondary hydrogen injection, Combust. Flame 214 (2020) 266–276, doi:10.1016/j.combustflame.2019.12.032.

[9] T. Schuller, S. Marragou, G. Oztarlik, T. Poinsot, L. Selle, Influence of hydrogen content and injection scheme on the describing function of swirled flames, Combust. Flame 240 (2022) 111974.

[10] D. Laera, P.W. Agostinelli, L. Selle, Q. Cazères, G. Oztarlik, T. Schuller, L. Gicquel, T. Poinsot, Stabilization mechanisms of CH4 premixed swirled flame enriched with a non-premixed hydrogen injection, Proc. Combust. Inst. 38 (4) (2021) 6355–6363.

[11] T. Lee, K.T. Kim, Combustion dynamics of lean fully-premixed hydrogen-air flames in a mesoscale multinozzle array, Combust. Flame 218 (2020) 234–246, doi:10.1016/j.combustflame.2020.04.024.

[12] H. Kang, K.T. Kim, Combustion dynamics of multi-element lean-premixed hydrogen-air flame ensemble, Combust. Flame 233 (2021) 111585, doi:10.1016/j.combustflame.2021.111585.

[13] T. Lee, K.T. Kim, High-frequency transverse combustion instabilities of lean-premixed multislit hydrogen-air flames, Combust. Flame 238 (2022) 111899, doi:10.1016/j.combustflame.2021.111899.

[14] L. Figura, J.G. Lee, B.D. Quay, D.A. Santavicca, The effects of fuel composition on flame structure and combustion dynamics in a lean premixed combustor, Volume 2: Turbo Expo 2007, ASMEDC, 2007, doi:10.1115/gt2007-27298.

[15] K.T. Kim, J.G. Lee, H.J. Lee, B.D. Quay, D.A. Santavicca, Characterization of forced flame response of swirl-stabilized turbulent lean-premixed flames in a gas turbine combustor, J. Eng. Gas Turbine Power 132 (4) (2010), doi:10.1115/1.3204532.

[16] D. Davis, P. Therkelsen, D. Littlejohn, R. Cheng, Effects of hydrogen on the thermo-acoustics coupling mechanisms of low-swirl injector flames in a model gas turbine combustor, Proc. Combust. Inst. 34 (2) (2013) 3135–3143, doi:10.1016/j.proci.2012.05.050.

[17] T. Guiberti, D. Durox, P. Scouflaire, T. Schuller, Impact of heat loss and hydrogen enrichment on the shape of confined swirling flames, Proc. Combust. Inst. 35 (2) (2015) 1385–1392, doi:10.1016/j.proci.2014.06.016.

[18] S. Shanbhogue, Y. Sanusi, S. Taamallah, M. Habib, E. Mokheimer, A. Ghoniem, Flame macrostructures, combustion instability and extinction strain scaling in swirl-stabilized premixed CH4/h2 combustion, Combust. Flame 163 (2016) 494–507, doi:10.1016/j.combustflame.2015.10.026.

[19] I. Chterev, I. Boxx, Effect of hydrogen enrichment on the dynamics of a lean technically premixed elevated pressure flame, Combust. Flame 225 (2021) 149–159, doi:10.1016/j.combustflame.2020.10.033.

[20] R. Mao, J. Wang, W. Lin, W. Han, W. Zhang, Z. Huang, Effects of flow-flame interactions on the stabilization of ultra-lean swirling CH4/H2/air flames, Fuel 319 (2022) 123619, doi:10.1016/j.fuel.2022.123619.

[21] E. Æsøy, J.G. Aguilar, S. Wiseman, M.R. Bothien, N.A. Worth, J.R. Dawson, Scaling and prediction of transfer functions in lean premixed H2/CH4 flames, Combust. Flame 215 (2020) 269–282, doi:10.1016/j.combustflame.2020.01.045.

[22] E. Æsøy, J.G. Aguilar, M.R. Bothien, N. Worth, J. Dawson, Acoustic-convective interference in transfer functions of methane/hydrogen and pure hydrogen flames, J. Eng. Gas Turbine Power (2021), doi:10.1115/1.4051960.

[23] E. Æsøy, H.T. Nygård, N.A. Worth, J.R. Dawson, Tailoring the gain and phase of the flame transfer function through targeted convective-acoustic interference, Combust. Flame 236 (2022) 111813, doi:10.1016/j.combustflame.2021.111813.

[24] E. Æsøy, T. Indlekofer, F. Gant, A. Cuquel, M.R. Bothien, J.R. Dawson, The effect of hydrogen enrichment, flame-flame interaction, confinement, and asymmetry on the acoustic response of a model can combustor, Combust. Flame 242 (2022) 112176, doi:10.1016/j.combustflame.2022.112176.

[25] E. Æsøy, The Effect of Hydrogen Enrichment on the Thermoacoustic Behaviour of Lean Premixed Flames, 2022 Ph.D. thesis.

[26] A. Ghani, W. Polifke, Control of intrinsic thermoacoustic instabilities using hydrogen fuel, Proc. Combust. Inst. 38 (4) (2021) 6077–6084, doi:10.1016/j.proci.2020.06.151.

[27] U. Krüger, J. Hüren, S. Hoffmann, W. Krebs, D. Bohn, Prediction of thermoacoustic instabilities with focus on the dynamic flame behavior for the 3a-series gas turbine of siemens KWU, Volume 2: Coal, Biomass and Alternative Fuels; Combustion and Fuels; Oil and Gas Applications; Cycle Innovations, American Society of Mechanical Engineers, 1999, doi:10.1115/99-gt-111.

[28] X. Han, J. Li, A.S. Morgans, Prediction of combustion instability limit cycle oscillations by combining flame describing function simulations with a thermoacoustic network model, Combust. Flame 162 (10) (2015) 3632–3647, doi:10.1016/j.combustflame.2015.06.020.

[29] T. Schuller, D. Durox, S. Candel, A unified model for the prediction of laminar flame transfer functions, Combust. Flame 134 (1–2) (2003) 21–34, doi:10.1016/s0010-2180(03)00042-7.

[30] G. Staffelbach, L. Gicquel, G. Boudier, T. Poinsot, Large eddy simulation of self excited azimuthal modes in annular combustors, Proc. Combust. Inst. 32 (2) (2009) 2909–2916, doi:10.1016/j.proci.2008.05.033.

[31] N. Noiray, D. Durox, T. Schuller, S. Candel, A unified framework for nonlinear combustion instability analysis based on the flame describing function, J. Fluid Mech. 615 (2008) 139–167.

[32] A.P. Dowling, S.R. Stow, Acoustic analysis of gas turbine combustors, J. Propuls. Power 19 (5) (2003) 751–764, doi:10.2514/2.6192.

[33] W. Polifke, Modeling and analysis of premixed flame dynamics by means of distributed time delays, Prog. Energy Combust. Sci. 79 (2020) 100845, doi:10.1016/j.pecs.2020.100845.

[34] B. Higgins, M. Mcquay, F. Lacas, J. Rolon, N. Darabiha, S. Candel, Systematic measurements of OH chemiluminescence for fuel-lean, high-pressure, premixed, laminar flames, Fuel 80 (1) (2001) 67–74, doi:10.1016/s0016-2361(00)00069-7.

[35] R. Balachandran, B. Ayoola, C. Kaminski, A. Dowling, E. Mastorakos, Experimental investigation of the nonlinear response of turbulent premixed flames to imposed inlet velocity oscillations, Combust. Flame 143 (1–2) (2005) 37–55, doi:10.1016/j.combustflame.2005.04.009.

[36] B. Schuermans, F. Guethe, D. Pennell, D. Guyot, C.O. Paschereit, Thermoacoustic modeling of a gas turbine using transfer functions measured under full engine pressure, J. Eng. Gas Turbine Power 132 (11) (2010), doi:10.1115/1.4000854.

[37] C.J. Dasch, One-dimensional tomography: a comparison of abel, onion-peeling, and filtered backprojection methods, Appl. Opt. 31 (8) (1992) 1146, doi:10.1364/ao.31.001146.

[38] D. Kim, J.G. Lee, B.D. Quay, D.A. Santavicca, K. Kim, S. Srinivasan, Effect of flame structure on the flame transfer function in a premixed gas turbine combustor, J. Eng. Gas Turbine Power 132 (2) (2010).

[39] V. Nair, G. Thampi, R. i. Sujith, Intermittency route to thermoacoustic instability in turbulent combustors, J. Fluid Mech. 756 (2014) 470–487, doi:10.1017/jfm.2014.468.

[40] D.G. Goodwin, H.K. Moffat, R.L. Speth, Cantera: an object-oriented software toolkit for chemical kinetics, thermodynamics, and transport processes. version 2.2.0, Zenodo (2015). doi:10.5281/ZENODO.48735.

[41] T. Komarek, W. Polifke, Impact of swirl fluctuations on the flame response of a perfectly premixed swirl burner, J. Eng. Gas Turbine Power 132 (6) (2010), doi:10.1115/1.4000127.

[42] P. Palies, D. Durox, T. Schuller, S. Candel, The combined dynamics of swirler and turbulent premixed swirling flames, Combust. Flame 157 (9) (2010) 1698–1717, doi:10.1016/j.combustflame.2010.02.011.

[43] M. Gatti, R. Gaudron, C. Mirat, T. Schuller, Impact of swirl and bluff-body on the transfer function of premixed flames, Proc. Combust. Inst. 37 (4) (2019) 5197–5204, doi:10.1016/j.proci.2018.06.148.

[44] R. Gaudron, M. Gatti, C. Mirat, T. Schuller, Flame describing functions of a confined premixed swirled combustor with upstream and downstream forcing, J. Eng. Gas Turbine Power 141 (5) (2019), doi:10.1115/1.4041000.

[45] J. Zhang, A. Ratner, Experimental study of the effects of hydrogen addition on the thermoacoustic instability in a variable-length combustor, Int. J. Hydrog. Energy 46 (29) (2021) 16086–16100, doi:10.1016/j.ijhydene.2021.02.063.

[46] M.P. Juniper, R. Sujith, Sensitivity and nonlinearity of thermoacoustic oscillations, Annu. Rev. Fluid Mech. 50 (1) (2018) 661–689, doi:10.1146/annurev-fluid-122316-045125.

[47] A.F. Seybert, D.F. Ross, Experimental determination of acoustic properties using a two-microphone random-excitation technique, J. Acoust. Soc. Am. 61 (5) (1977) 1362–1370, doi:10.1121/1.381403.

[48] W. Polifke, C. Lawn, On the low-frequency limit of flame transfer functions, Combust. Flame 151 (3) (2007) 437–451, doi:10.1016/j.combustflame.2007.07.005.